

Efficient Cu—Co Dual-Sites in Cobalt Oxide Nanoboxes for Electrocatalytic Reduction of Low-Concentration NO to NH₃

Dongdong Wang, Guilan Fan, Zhihao Pei, Deyan Luan, Xiaojun Gu,*
and Xiong Wen David Lou*

The electrocatalytic conversion of nitric oxide (NO) to ammonia (NH₃) epitomizes an advanced approach in NH₃ synthesis, crucial for efficiently converting low-concentration industrial NO exhaust and contributing significantly to environmental preservation. Catalyst design remains one pivotal element in addressing this challenge. Here, efficient Cu—Co dual active sites embedded in hollow cobalt oxide nanoboxes are created for the electrocatalytic low-concentration NO reduction reaction (NORR). Cu-modified cobalt oxide (Cu-Co₃O₄) and its heterophase interface with copper oxide (Cu-Co₃O₄/CuO) both exhibit over 93% Faraday efficiency for NH₃ synthesis, with a yield reaching up to 59.10 μg h⁻¹ mg_{cat}⁻¹ at -0.4 V versus reversible hydrogen electrode by utilizing simulated industrial NO exhaust (1 vol %) as the feedstock, surpassing those of pure cobalt oxide and some reported catalysts. Theoretical calculations and NO temperature-programmed desorption experiments demonstrate that the incorporation of Cu significantly enhances NO adsorption and reduces the energy barrier of the rate-determining step. The integration of Cu-Co₃O₄ and Cu-Co₃O₄/CuO within the cathode of the Zn—NO battery demonstrates a notable power density of 2.02 mW cm⁻², highlighting a propitious direction for investigating highly efficient conversion of low-concentration NO exhaust gas.

1. Introduction

The growing importance of health implications, nitrogen cycle disruptions, and environmental issues (such as acid rain, photochemical smog, and ozone depletion) arising from nitric oxide (NO) emissions in industrial and vehicle exhaust is drawing the focus of researchers from diverse fields.^[1–3] Efforts are actively underway to tackle these challenges using a range of

innovative methods and strategic approaches.^[4,5] Despite being the forefront technology, selective catalytic reduction fails to meet scientists' expectations due to its stringent conditions and substantial consumption of valuable chemicals.^[6,7] In the past five years, electrochemical NO conversion technology driven by renewable energy has emerged as a new trend due to its environmental friendliness and straightforward controllability.^[8–10] On the one hand, it enables the efficient removal of NO emissions, and on the other hand, it facilitates the targeted synthesis of high-value chemicals.^[11–13] Ammonia (NH₃), a critical chemical, plays an indispensable role in agricultural sustainability and national strategic development.^[14,15] Currently, the electrochemical nitrogen reduction method is seen as a promising alternative to the traditional Haber-Bosch process, which is characterized by significant energy consumption and greenhouse gas emissions.^[16,17] However, it has been constrained by low NH₃ production performance due to the extreme inertness of

nitrogen molecules.^[18,19] Consequently, researchers in the nitrogen cycle field have been exploring novel ammonia synthesis approaches.^[20–22] Since 2020, Xiao's group pioneered the electrocatalytic NO reduction reaction (NORR) to produce ammonia, sparking considerable interest among researchers.^[23] The current focus and challenge lie in designing high-performance electrocatalysts.^[24,25]

At present, numerous electrocatalysts have been engineered for electrocatalytic NO reduction in ammonia synthesis, primarily including Cu foam,^[23] Co nanoparticles,^[26] and CuFe-450.^[27] Even precious metal catalysts like Ag nanostructure,^[28] RuGa,^[29] and Ru_{0.05}Cu_{0.95} have also been employed.^[30] It is noteworthy that these investigations have predominantly concentrated on electrocatalytic reduction of high-concentration NO (>10 vol %). Given the significantly lower NO concentrations (<5 vol %) derived from industrial emissions and plasma-activated nitrogen, the exploration of low-concentration or industrially simulated NO exhaust electrocatalytic conversion holds practical importance.^[31] Although Cu is the most active metal catalyst for NORR at high concentrations, its Faraday efficiency is less than 10% at low concentrations.^[32] This is mainly because the mass transfer and adsorption of NO gas on the catalyst surface becomes difficult

D. Wang, Z. Pei, D. Luan, X. W. D. Lou
Department of Chemistry
City University of Hong Kong
83 Tat Chee Avenue, Kowloon, Hong Kong 999077, China
E-mail: david.lou@cityu.edu.hk

G. Fan, X. Gu
School of Chemistry and Chemical Engineering
Inner Mongolia University
Hohhot 010021, China
E-mail: xiaojun.gu@imu.edu.cn

The ORCID identification number(s) for the author(s) of this article can be found under <https://doi.org/10.1002/adma.202504497>

DOI: 10.1002/adma.202504497

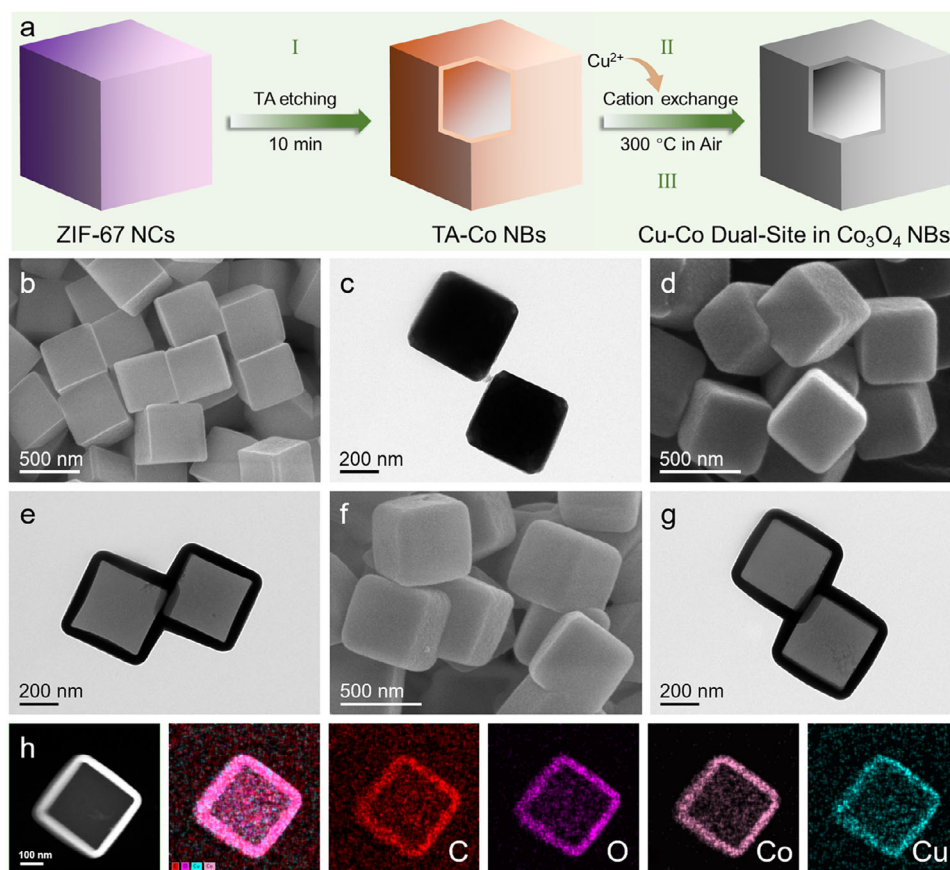


Figure 1. a) Schematic diagram of the synthesis process for Cu- Co_3O_4 NBs and Cu- $\text{Co}_3\text{O}_4/\text{CuO}$ NBs: (I) etching ZIF-67 NCs with TA to obtain TA-Co NBs, (II) introducing Cu through cation exchange, (III) calcination to form the corresponding oxides. b) SEM image and c) TEM image of the ZIF-67 NCs. d) SEM image and e) TEM image of the TA-Co NBs. f) SEM image and g) TEM image of the TA-CuCo NBs. h) HAADF-STEM image and the corresponding elemental mapping images of a TA-CuCo NB.

at low concentrations. Subsequently, researchers tried to develop various strategies to design catalysts to address these two challenges, including defect engineering,^[33] strain engineering,^[34] and composition regulation. Zhang's group achieved efficient conversion of low-concentration NO by constructing porous carbon on the surface of Cu nanowire arrays to improve NO diffusion and coverage.^[35] Considering that metallic Co and its oxides are the active components for NO conversion and NH_3 synthesis, we recently implanted Ru into Co nanoparticles to induce phase transition to enhance NO adsorption capacity, thereby promoting NORR activity.^[36,37] Porous micro/nanostructures characterized by intricate hollow configurations maximize active site exposure, thereby amplifying mass diffusion and culminating in superior electrocatalytic activity.^[38] Therefore, the strategic design and synthesis of electrocatalysts with NO adsorption capacities within the active components ensconced in hollow structures represent a pioneering pathway toward a novel paradigm in electrocatalytic NORR for ammonia synthesis.

In this work, we report an efficient Cu-Co dual-site system embedded in hollow cobalt oxide nanoboxes for ammonia synthesis through a synergistic approach involving acid etching and cation exchange strategies. Cu-modified cobalt oxide ($\text{Cu-Co}_3\text{O}_4$) and its heterophase interface with copper oxide ($\text{Cu-Co}_3\text{O}_4/\text{CuO}$)

both exhibit over 93% Faraday efficiency for NH_3 synthesis, with a yield reaching up to $59.10 \mu\text{g h}^{-1} \text{mg}_{\text{cat}}^{-1}$ at -0.4 V versus reversible hydrogen electrode (vs. RHE) at a low NO concentration of 1 vol % (1% thereafter), exceeding pure cobalt oxide and some reported catalysts under similar testing conditions. The integrated Zn-NO system demonstrated a power density of 2.02 mW cm^{-2} and an NH_3 yield of $17.66 \mu\text{g h}^{-1} \text{mg}_{\text{cat}}^{-1}$. Theoretical calculation results prove that Cu modification significantly optimizes the electronic structure of the catalyst and lowers the energy barrier of the rate-determining step. These findings offer novel insights into the design of catalysts for the electrochemical reduction of low-concentration NO.

2. Results and Discussion

Inspired by the preceding discussion, as illustrated in Figure 1a, we fabricated cobalt oxide nanoboxes (NBs) embedding Cu-Co bimetallic sites within hollow structures. Specifically, highly uniform zeolitic imidazolate framework-67 nanocubes (ZIF-67 NCs) were initially synthesized as the starting material through a modification of the method previously reported by our group (Figures S1 and S2, Supporting Information).^[39] Scanning electron

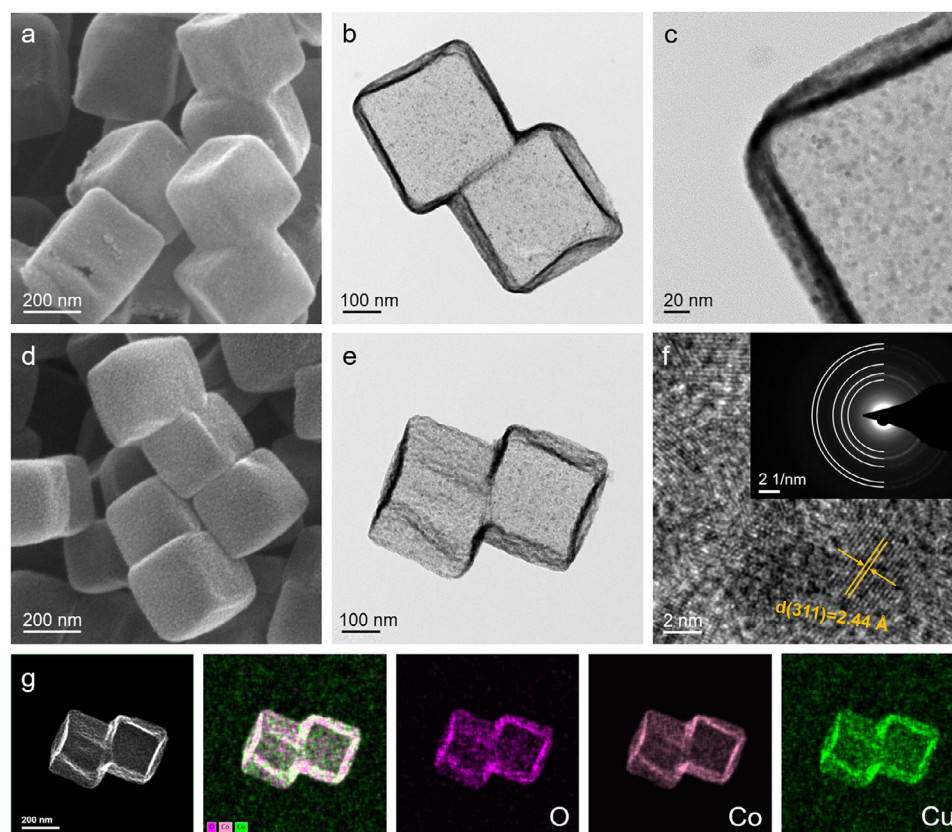


Figure 2. a) SEM image, b) TEM image and c) partially enlarged TEM image of the Co_3O_4 NBs. d) SEM image, e) TEM image and f) HRTEM image of $\text{Cu-Co}_3\text{O}_4$ NBs, the inset in (f) is the SAED pattern. g) HAADF-STEM image and the corresponding elemental mapping images of $\text{Cu-Co}_3\text{O}_4$ NBs.

microscopy (SEM) and transmission electron microscopy (TEM) images showed that the average size of ZIF-67 NCs was about 480 nm (Figure 1b,c). Then, ZIF-67 NCs were etched by tannic acid (TA) to obtain hollow NBs. X-ray diffraction (XRD), SEM, and TEM results showed that TA- Co NBs were successfully synthesized (Figures S3 and S4, Supporting Information), characterized by an intact structure and a relatively smooth surface (Figure 1d,e). The resulting TA- Co NBs were further subject to cation exchange with Cu^{2+} to transform into TA- CuCo NBs, preserving the original hollow structure while the surface became rough (Figure 1f,g). The high-angle annular dark-field scanning transmission electron microscopy (HAADF-STEM) image, complemented by elemental mapping images, illustrated a uniform distribution of Cu, Co, O, and C elements on a single TA- CuCo NB (Figure 1h). The associated energy-dispersive X-ray spectroscopy (EDS) spectrum further validated the presence of these elements (Figure S5, Supporting Information).

Finally, by varying the content of the metal Cu and calcining in air, we obtained pure cobalt oxide (Co_3O_4) and a series of cobalt oxides embedded with Cu–Co bimetallic sites (samples obtained at a Cu salt concentration of 0.625 mM were denoted as $\text{Cu-Co}_3\text{O}_4$). As the concentration of the metal salt increased, the material transitioned into a heterogeneous structure comprising $\text{Cu-Co}_3\text{O}_4$ and CuO (samples obtained at a Cu salt concentration of 2.5 mM were labeled as $\text{Cu-Co}_3\text{O}_4/\text{CuO}$). The two experimental conditions actually represent the same cation

exchange approach, with the only variation being the concentration of Cu metal salt (0.625 mM for $\text{Cu-Co}_3\text{O}_4$ and 2.5 mM for $\text{Cu-Co}_3\text{O}_4/\text{CuO}$). The subsequent calcination was applied to all samples as the final step. Therefore, the only variable across samples was the Cu loading amount, with low concentrations producing $\text{Cu-doped Co}_3\text{O}_4$ phases and high concentrations yielding $\text{Cu-Co}_3\text{O}_4/\text{CuO}$ heterostructures. The results indicated that the hollow structure of Co_3O_4 was well maintained without obvious aggregation and collapse, as evidenced from an open NB (Figure 2a; Figure S6a,b, Supporting Information). TEM images further demonstrated the hollow structure with a wall thickness of ≈ 20 nm (Figure 2b). Notably, the surface of the nanocubes was assembled from ultrafine oxide nanoparticles, establishing a porous network between them that was conducive to promoting the exposure of active sites and enhancing substance diffusion (Figure 2c). After the introduction of Cu elements, the morphology and structure of $\text{Cu-Co}_3\text{O}_4$ were effectively retained (Figure 2d,e). High-resolution TEM (HRTEM) image revealed a lattice spacing of 2.44 Å, corresponding to the (311) crystal plane (Figure 2f). The selected area electron diffraction (SAED) pattern sequentially can be indexed to the (220), (311), (400), (511), and (440) crystal planes from the inside to the outside. The HAADF-STEM image, accompanied by elemental mapping images, revealed uniform dispersion of Cu, Co, and O elements across the $\text{Cu-Co}_3\text{O}_4$ NBs (Figure 2g). These morphological and structural features were consistent with those of Co_3O_4 NBs

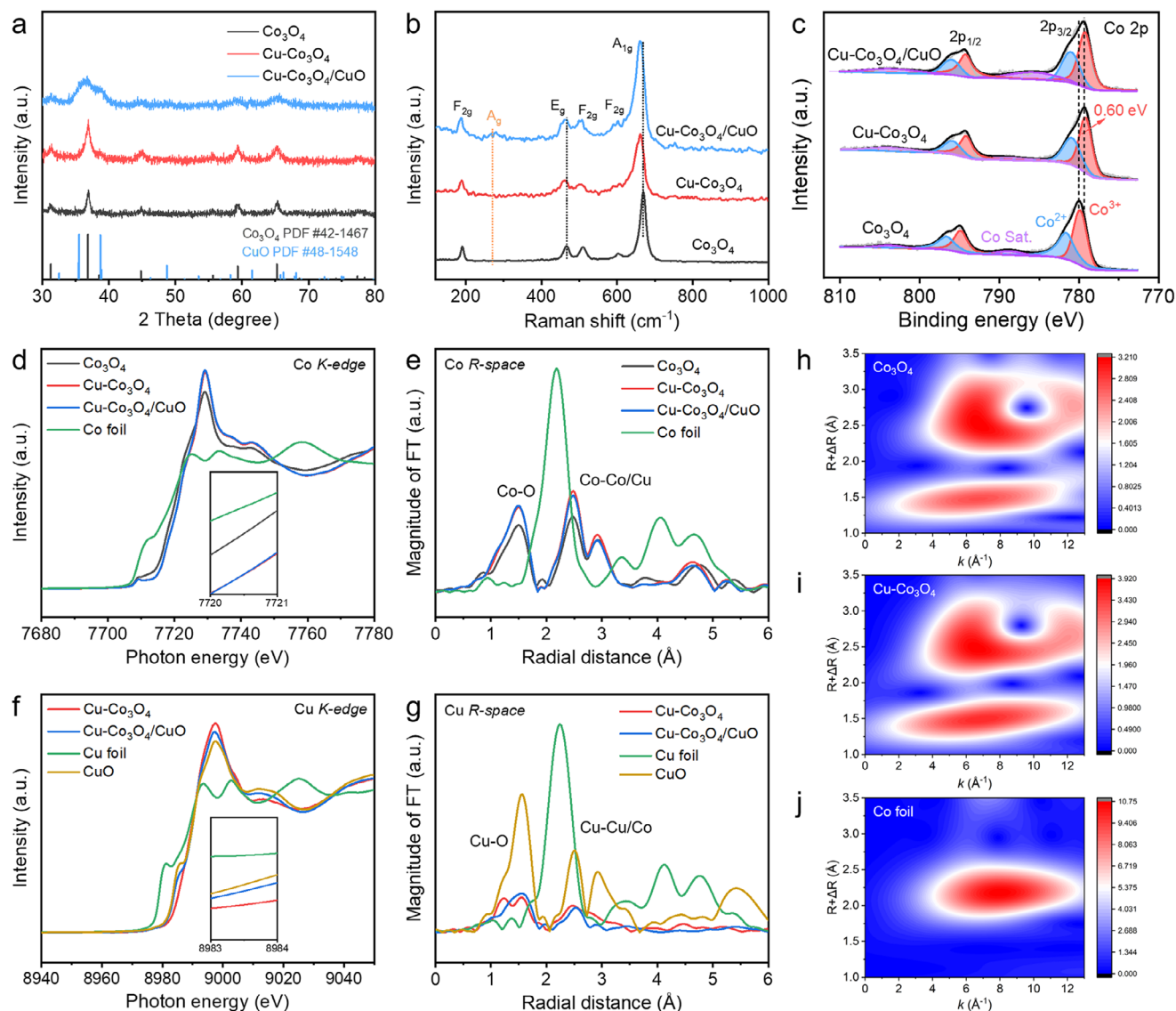


Figure 3. a) XRD patterns, b) Raman spectra and c) Co 2p XPS spectra of the Co_3O_4 NBs, $\text{Cu-Co}_3\text{O}_4$ NBs, and $\text{Cu-Co}_3\text{O}_4/\text{CuO}$ NBs. d) Normalized Co K-edge XANES spectra and e) the corresponding Fourier transform EXAFS spectra of the Co_3O_4 NBs, $\text{Cu-Co}_3\text{O}_4$ NBs, $\text{Cu-Co}_3\text{O}_4/\text{CuO}$ NBs, and reference samples. f) Normalized Cu K-edge XANES spectra and g) the corresponding Fourier transform EXAFS spectra of the Co_3O_4 NBs, $\text{Cu-Co}_3\text{O}_4$ NBs, $\text{Cu-Co}_3\text{O}_4/\text{CuO}$ NBs, and reference samples. WT of k^3 -weighted Co K-edge of the h) Co_3O_4 NBs, i) $\text{Cu-Co}_3\text{O}_4$ NBs, and j) Co foil.

(Figure S6c–e, Supporting Information), $\text{Cu-Co}_3\text{O}_4$ NBs with different Cu/Co ratios (Figures S7–S9, Supporting Information), and $\text{Cu-Co}_3\text{O}_4/\text{CuO}$ NBs (Figures S10–S13, Supporting Information). Notably, the lattice spacing of 2.44 and 2.53 Å corresponded to the (311) crystal plane of $\text{Cu-Co}_3\text{O}_4$ and the (002) crystal plane of CuO , respectively. In the SAED pattern, additional diffraction information was successively correlated with the (002) and (20-2) crystal plane of CuO from the inner to the outer regions. These results further confirmed the formation of the $\text{Cu-Co}_3\text{O}_4/\text{CuO}$ heterophase structures. Inductively coupled plasma optical emission spectroscopy results indicated that the Cu/Co atomic ratios in $\text{Cu-Co}_3\text{O}_4$ and $\text{Cu-Co}_3\text{O}_4/\text{CuO}$ were 0.19:1 and 1.47:1, respectively, and EDS also confirmed the presence of these elements (Table S1; Figure S14, Supporting Information).

XRD was utilized to identify the crystalline phase details of the catalysts. At lower Cu implantation levels, the catalyst exhibited a typical spinel oxide structure (Figure S15, Supporting Information). Furthermore, the synchrotron radiation powder XRD with robust signal resolution provided additional validation of these observations (Figure S16, Supporting Information). However, when the metal salt concentration exceeded 2.5 mM, a $\text{Cu-Co}_3\text{O}_4/\text{CuO}$ heterogeneous phase structure emerged, consistent with the HRTEM results mentioned above (Figure 3a). Raman spectra of pure Co_3O_4 also confirmed a typical spinel structure with A_{1g} , F_{2g} , E_g , F_{2g} , F_{2g} peaks.^[40] The redshift of the E_g and A_{1g} peaks in the Raman spectra of $\text{Cu-Co}_3\text{O}_4$ and $\text{Cu-Co}_3\text{O}_4/\text{CuO}$ indicated the insertion of Cu into Co_3O_4 .^[41] A peak around 270 cm^{-1} emerged in $\text{Cu-Co}_3\text{O}_4/\text{CuO}$, indicating the presence of the

A_g peak in CuO and confirming the successful formation of the heterogeneous structure (Figure 3b).^[42] Furthermore, a heterogeneous structure was observed when the metal salt concentration surpassed 2.5 mM, aligning with XRD analysis (Figure S17, Supporting Information). The X-ray photoelectron spectroscopy (XPS) survey spectra reveal the presence of Co, Cu, and O elements on the surface of catalysts (Figure S18a, Supporting Information). As shown in Figure 3c, the peaks at approximately 779.86, 781.62, and 788.68 eV in the Co 2p XPS were attributed to Co^{3+} , Co^{2+} , and satellite peaks (Co Sat.), respectively. Compared with Co_3O_4 NBs, the binding energy of Co 2p in $Cu-Co_3O_4$ NBs and $Cu-Co_3O_4/CuO$ NBs negatively shifted by ≈ 0.6 eV, indicating electron transfer from Co to Cu atoms upon the introduction of Cu elements.^[43] Consequently, the integration of Cu into Co_3O_4 NBs led to a notable cooperative charge effect, modifying their electronic configurations and possibly boosting electrochemical activity. In the Cu 2p XPS spectra (Figure S18b, Supporting Information), strong satellite peak signals were observed, which were typical characteristics of Cu^{2+} .

X-ray absorption near-edge structure (XANES) and X-ray absorption fine structure (EXAFS) were examined for investigating the coordination environment and electronic structure information of electrocatalysts. Compared with Co_3O_4 NBs, the absorption edges in the Co K-edge spectra of $Cu-Co_3O_4$ NBs and $Cu-Co_3O_4/CuO$ NB shift toward higher energy, indicating an increase in the oxidation state of Co by introducing Cu atoms (Figure 3d). The corresponding EXAFS spectra of Co K-edge show that the three catalysts have similar coordination environments, indicating that Cu modification does not significantly alter the coordination of Co atoms (Figure 3e). Specifically, the three main peaks in the EXAFS spectrum are attributed to Co–O, octahedral Co–Co and tetrahedral Co–Co/Cu bonds, respectively.^[44] In the Cu K-edge XANES spectra (Figure 3f), compared with the CuO reference, the shoulder peak at 8985 eV of $Cu-Co_3O_4$ NBs disappears, and the adsorption edge shifts to higher energy, indicating that Cu implantation results in a distinct state rather than the formation of independent CuO. In $Cu-Co_3O_4/CuO$ NBs, the adsorption edge is only slightly more positive than that of the CuO reference, accompanied by the appearance of a shoulder peak, suggesting the formation of a heterophase interface. In the corresponding Cu K-edge EXAFS spectra (Figure 3g), the $Cu-Co_3O_4$ NBs sample only exhibits peaks at 1.54 and 2.50 Å, corresponding to Cu–O and Cu–Cu bonds, respectively. The disappearance of the peak at 2.93 Å indicates the differences in their coordination environments from the CuO reference and the successful insertion of Cu into Co_3O_4 NBs. However, a small peak emerges at 2.93 Å for $Cu-Co_3O_4/CuO$ NBs, suggesting the formation of CuO. The wavelet transform (WT) of k^3 -weighted Co K-edge EXAFS spectra reflects information about Co–O and Co–Co bonds that align with the EXAFS spectra (Figure 3h–j). These results indicate that Cu implantation effectively regulates the electronic structure and coordination environment of Co_3O_4 NBs.

A sealed H-shaped cell with the typical three-electrode system was used to assess the electrochemical ammonia synthesis activity via NORR in a 0.5 M Na_2SO_4 electrolyte. Carbon paper (CP) coated with catalyst was used as the working electrode. Before conducting the test, the linear sweep voltammetry (LSV) was executed multiple times until a stable state was established. A larger

current was observed when 1% NO substrate was introduced into the electrolyte, indicating that electrochemical NORR occurred (Figure 4a; S19, Supporting Information). The generated ammonia was quantitatively detected by a colorimetric method (Figure S20, Supporting Information). Before each potentiostatic test, high-purity He gas was passed through to purify the electrolyte by displacing oxygen. The electrochemical NORR performance of $Cu-Co_3O_4$ NBs for ammonia production was evaluated in the range of -0.4 – 0.8 V vs. RHE (Figure S21, Supporting Information), and the results showed a Faraday efficiency of 94.13% and an NH_3 yield of $54.28 \mu g h^{-1} mg_{cat}^{-1}$ (Figure 4b). Detection measurements revealed no trace of other liquid products, including hydrazine (Figures S22 and S23, Supporting Information) and hydroxylamine (Figures S24 and S25, Supporting Information). To highlight the advantages of the Cu–Co dual active sites, the NORR performance of pure Co_3O_4 NBs was also assessed, revealing a lower Faraday efficiency of 75.29% and an NH_3 production rate of $24.05 \mu g h^{-1} mg_{cat}^{-1}$ (Figures S26 and S27, Supporting Information). Furthermore, it was found that the $Cu-Co_3O_4/CuO$ NBs with heterophase interface also exhibited NH_3 synthesis performance comparable to $Cu-Co_3O_4$ NBs (Faraday efficiency, 93.19%; yield rate, $59.10 \mu g h^{-1} mg_{cat}^{-1}$), surpassing both pure Co_3O_4 NBs and some catalysts in the literature under similar conditions (Figures S28 and S29; Table S2, Supporting Information). These electrochemical experimental results indicated that the Cu–Co dual-site catalyst can enhance NORR performances through a bimetallic synergy effect.^[45] Subsequently, we delved into the impact of different Cu/Co ratios in the $Cu-Co_3O_4$ NBs and $Cu-Co_3O_4/CuO$ NBs on the NORR performance (Figures S30–S32, Supporting Information). As the Cu content increased, NORR performance increased first and then decreased. There was no significant decay in the NH_3 production rate and Faraday efficiency on $Cu-Co_3O_4$ NBs at -0.4 V vs. RHE over six cycles, demonstrating the stability of the materials (Figure 4c; Figures S33 and S34, Supporting Information). To obtain rigorous stability data, we conducted a 120-h NORR stability test at -0.4 V vs. RHE (Figure S35, Supporting Information). The results showed negligible current decay, with the Faraday efficiency and yield of NH_3 maintained at 57.38% and $34.06 \mu g h^{-1} mg_{cat}^{-1}$, respectively. Post-stability test characterizations revealed that $Cu-Co_3O_4$ NBs retained their original phase structure and composition (Figure S36; Table S3, Supporting Information). The performance degradation observed may be attributed to localized microstructural changes in the catalysts, as evidenced by TEM analysis showing partial structural collapse of $Cu-Co_3O_4$ NBs (Figure S37, Supporting Information). A range of meticulously designed experiments was executed under diverse conditions to validate the source of the NH_3 derived from NORR, unaffected by external influences (Figure 4d; Figure S38, Supporting Information). By conducting NORR separately in open (1% NO+Air) and sealed (NO) chambers to test the reliability of our measurement data, a higher reduction current, increased NH_3 production, nitrate (NO_3^-), and nitrite (NO_2^-) yield were obtained (Figures S39 and S40, Supporting Information). This was attributed to the facile chemical reaction of NO with oxygen and water in an open system, providing NO_3^- (18.10 ppm) and NO_2^- (21.87 ppm) as nitrogen sources for NH_3 synthesis (Figure 4e; Figures S41–S44, Supporting Information). As shown in Figure 4f, NO temperature-programmed desorption (NO-TPD) experiments were employed to investigate the

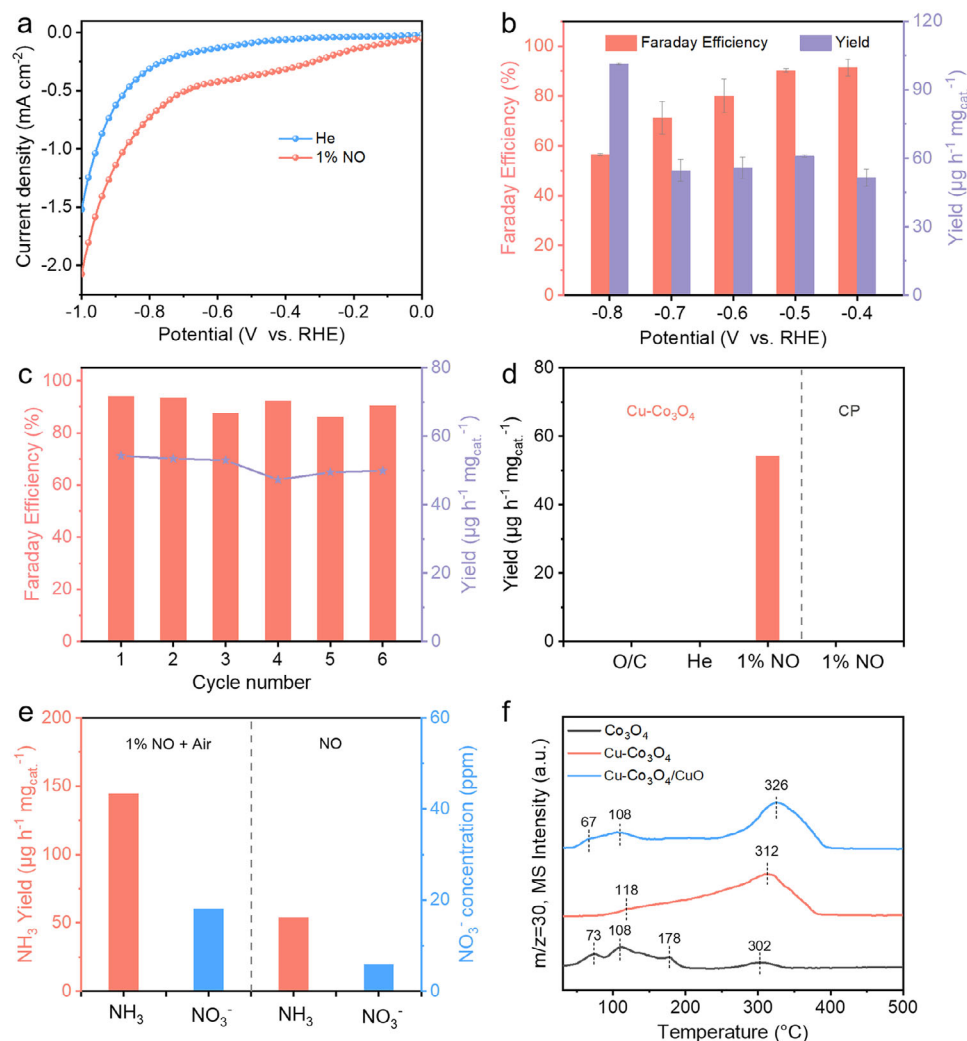


Figure 4. a) LSV curves of the Cu-Co₃O₄ NBs in He and 1% NO-saturated 0.5 M Na₂SO₄. b) Faraday efficiency and yield rate of NH₃ at each given potential over Cu-Co₃O₄ NBs. c) Faraday efficiency and yield rate of NH₃ in six successive cycles over Cu-Co₃O₄ NBs at -0.4 V vs. RHE. d) Electrochemical NORR activity over Cu-Co₃O₄ NBs and CP under various conditions (O/C denotes the elimination of the external potential). e) NH₃ yield and nitrate concentration in various testing environments over Cu-Co₃O₄ NBs at -0.4 V vs. RHE. f) NO-TPD spectra of the Co₃O₄ NBs, Cu-Co₃O₄ NBs, and Cu-Co₃O₄/CuO NBs.

NO adsorption behavior of the electrocatalysts. Both Cu-Co₃O₄ NBs and Cu-Co₃O₄/CuO NBs exhibited significantly stronger NO adsorption capabilities compared to pure Co₃O₄ NBs, particularly evidenced by prominent chemical adsorption peaks (200–400 °C), indicating that the incorporation of Cu significantly enhanced the NO adsorption capacity in cobalt oxides.

To elucidate the intricacies of the catalytic mechanism, density functional theory (DFT) calculations were conducted. Based on the physical characterization results, the Co₃O₄(311), Cu-Co₃O₄(311), and Cu-Co₃O₄(311)/CuO(002) surfaces were chosen for subsequent theoretical studies (Figure S45, Supporting Information). The adsorption energies of NO on different adsorption sites of the three catalysts were considered (Figure S46, Supporting Information). Theoretical calculations reveal that the NO adsorption energies on the surfaces of Co₃O₄, Cu-Co₃O₄, and Cu-Co₃O₄/CuO are -1.81, -1.95, and -2.27 eV, respectively (Figure S47, Supporting Information), indicating a significant enhance-

ment in NO adsorption capacity after constructing the Cu-Co dual sites. These results are in excellent agreement with the NO-TPD experimental results. Upon the incorporation of Cu, a significant accumulation of charge density between Co adsite and N atom is observed on the NO adsorbate over Cu-Co₃O₄ and Cu-Co₃O₄/CuO, while the electron density at the N atom is notably depleted (Figure 5a). This indicates that the addition of Cu atom or CuO in Co₃O₄ facilitates a higher degree of NO molecule activation compared to pure Co₃O₄. The accumulation of charge density around the Cu atoms in Cu-Co₃O₄ and Cu-Co₃O₄/CuO suggests electron transfer between Co and Cu, which is consistent with the XPS analysis. As illustrated in Figure 5b–d, by analyzing the projected density of states (PDOS) of the catalysts before and after NO adsorption, the interactions between the atomic orbitals of NO molecule and metal sites were investigated. The orbital energy level decreases and the peak intensity weakens for NO due to the electrons transfer from N to Co atoms

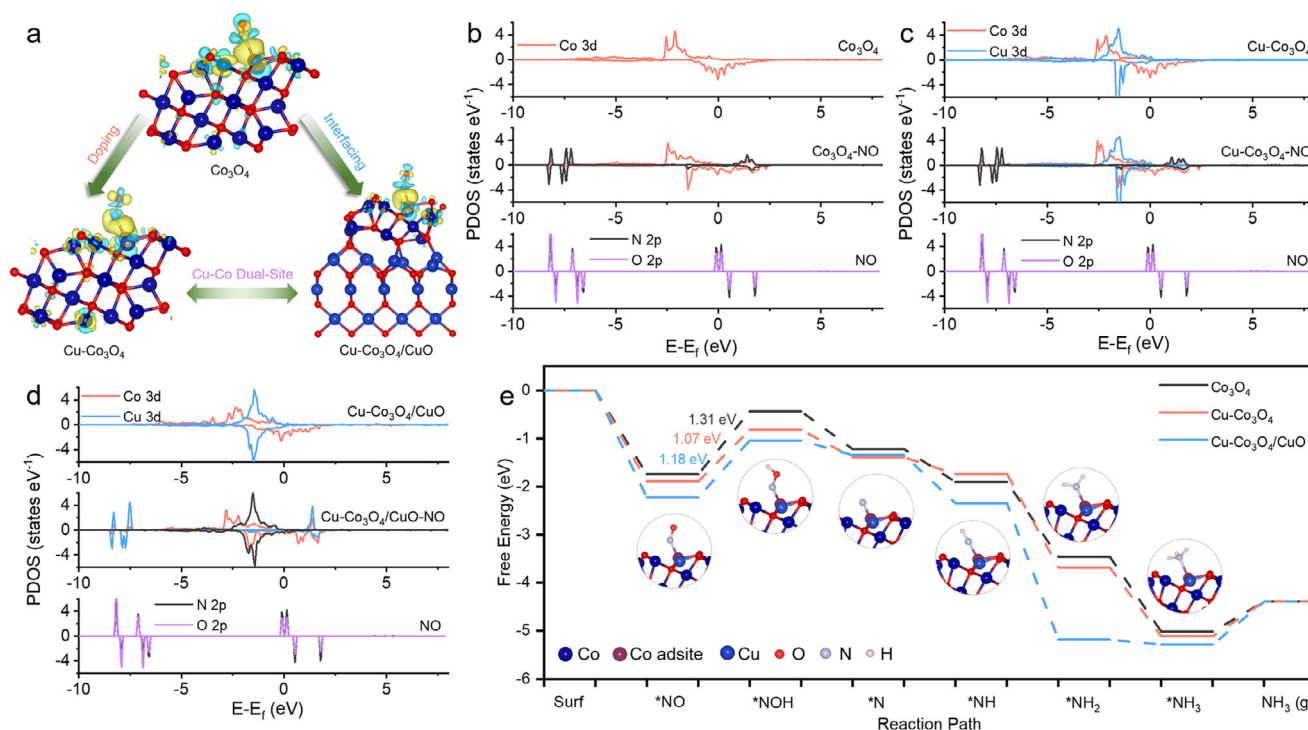


Figure 5. a) The charge density difference of *NO adsorbed on the Co₃O₄, Cu-Co₃O₄, and Cu-Co₃O₄/CuO. The accumulation and depletion of the electron density are marked in yellow and cyan, respectively. The PDOS of b) Co₃O₄, c) Cu-Co₃O₄, and d) Cu-Co₃O₄/CuO before and after the adsorption of NO. e) The free energy diagram of NORR on the Co₃O₄, Cu-Co₃O₄, and Cu-Co₃O₄/CuO. The inset shows the optimized geometry structures of NORR intermediates over Cu-Co₃O₄.

under the interaction with three catalysts, and the more significant change for orbital energy of NO adsorbed on Cu-Co₃O₄/CuO is observed. The higher energy level for Cu 3d orbital of Cu atom near Co adsite in Cu-Co₃O₄/CuO compared to that in Cu-Co₃O₄ indicates the electron transfer from Co to Cu, which leads to the stronger orbital interaction between Co and N atoms in Cu-Co₃O₄/CuO. In Figure 5e (and Figures S48 and S49, Supporting Information), the free energy profiles for the NORR process on Co₃O₄, Cu-Co₃O₄, and Cu-Co₃O₄/CuO are depicted. Building on insights from our earlier research and supported by recent theoretical investigations,^[36,46] the first protonation step from *NO to *NOH is frequently identified as a pivotal factor and the potential-determining step in the NORR process. As a result, the Cu-Co₃O₄ demonstrates a significantly lower energy barrier (1.07 eV) compared to the Cu-Co₃O₄/CuO (1.18 eV) and Co₃O₄ (1.31 eV), highlighting a notable improvement in catalytic efficiency for the Cu-Co₃O₄ and Cu-Co₃O₄/CuO. The hydrogen evolution reaction activity of these catalysts was also evaluated through theoretical calculations (Figure S50, Supporting Information), and the results demonstrated the high selectivity of Cu-Co₃O₄ catalyst for NH₃. These theoretical studies are consistent with our experimental results.

A proof-of-concept Zn-NO battery with catalysis-type mechanisms was assembled using Cu-Co₃O₄ NBs as the cathode to investigate the NORR performance. During the battery discharge process, the Zn-NO electrochemistry implements electrochemical NO reduction driven by Zn dissolution. Compared to conventional electrolytic NO-to-ammonia conversion processes, the

Zn-NO battery demonstrates specific advantages including self-powered operation, simultaneous electricity generation and valuable ammonia production, making it particularly suitable for portable and distributed ammonia synthesis applications (Table S4, Supporting Information). This setup aimed to explore the synergy of electricity generation, NO removal, and NH₃ production within a single system (Figure 6a). The assembled Zn-NO batteries with Cu-Co₃O₄ NBs and Cu-Co₃O₄/CuO NBs as electrodes output power densities of 1.58 and 2.02 mW cm⁻², respectively (Figure 6b), which are significantly higher than those of bare CP, Co₃O₄ NBs, and most reported catalytic materials in Zn-NO/N₂ batteries (Figure 6c; Table S5, Supporting Information). Although the power density obtained in Zn-low-concentration NO batteries is considerable, it is still not superior compared with conventional Zn-air batteries (>150 mW cm⁻²), Zn-NO₃⁻ batteries (>5 mW cm⁻²), and Zn-pure NO batteries (>2 mW cm⁻²).^[47,48] The development of some gas enrichment strategies and three-phase interface optimization methods will be beneficial to improve the performance of Zn-low-concentration NO batteries in future research. The Cu-Co₃O₄ NBs-based Zn-NO battery exhibits an open-circuit voltage (OCV) of 2.10 V vs. Zn, aligning closely with the polarization curve (Figure 6d). It exhibits stable discharge capacity in the current density range from 1 to 5 mA cm⁻² and shows an ammonia yield of 17.66 μg h⁻¹ mg_{cat}⁻¹ at 5 mA cm⁻² (Figure 6e,f; Figure S51, Supporting Information). Therefore, these results indicate that the Zn-NO battery might be a good solution for the efficient utilization of waste NO gas. Considering that the key issue in the operation of Zn-NO batteries

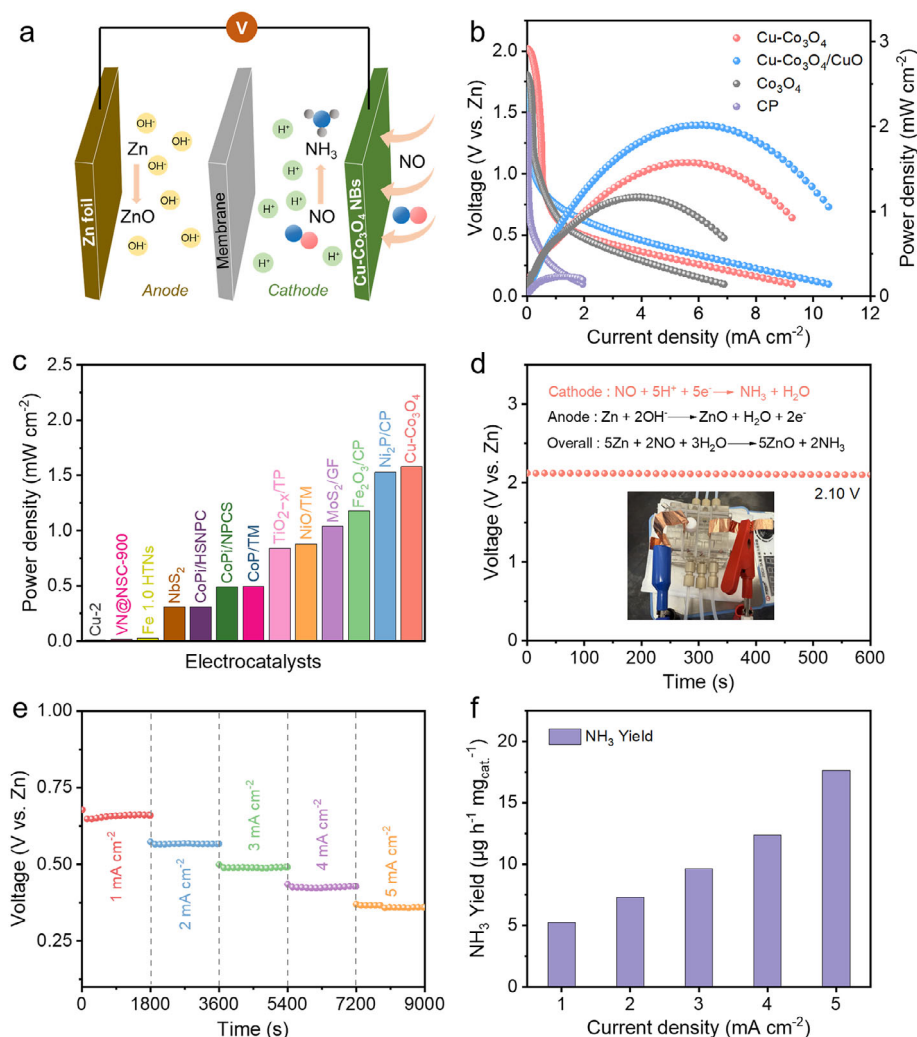


Figure 6. a) Schematic diagram of the designed Zn-NO battery. b) Polarization curves and power density curves of the Co₃O₄ NBs, Cu-Co₃O₄ NBs, Cu-Co₃O₄/CuO NBs, and CP-based Zn-NO batteries. c) Comparison of power density of the Cu-Co₃O₄ NBs-based Zn-NO battery and many reported Zn-NO/N₂ batteries. d) OCV of the Cu-Co₃O₄ NBs-based Zn-NO battery. The inset is the corresponding optical photograph. e) Continuous discharge curves of the Cu-Co₃O₄ NBs-based Zn-NO battery at various current densities. f) NH₃ yield at different current densities.

is the stability of NO supply, which directly affects the output of Zn-NO batteries. Zn-NO batteries can maintain their function by switching reaction paths or system design when NH₃ generation halts. Specifically, if NO is depleted, oxygen or air can be introduced as a substrate to switch to Zn-air batteries mode, but this transition requires a dual-functional cathode design. This emerging Zn-NO battery shows application potential in areas such as atmospheric pollutant control, distributed ammonia production, and temporary power supply.

3. Conclusion

In summary, efficient Cu-Co dual-sites in hollow cobalt oxide nanoboxes have been developed for the electrocatalytic reduction of low-concentration NO to NH₃. Both Cu-Co₃O₄ NBs and Cu-Co₃O₄/CuO NBs with Cu modification exhibit Faraday efficiency greater than 93% and ammonia yields up to 59.10 μg h⁻¹

mg_{cat}⁻¹ at -0.4 V vs. RHE, surpassing that of 75.29% and 24.05 μg h⁻¹ mg_{cat}⁻¹ for the bare Co₃O₄ NBs. DFT calculations and NO-TPD results demonstrate that Cu modification enhances NO adsorption and activation while lowering the energy barrier of the rate-determining step. In a proof-of-concept demonstration, the assembled Zn-NO batteries utilizing Cu-Co₃O₄ NBs and Cu-Co₃O₄/CuO NBs as electrode materials showcase power densities of 1.58 and 2.02 mW cm⁻², respectively, with an NH₃ yield of 17.66 μg h⁻¹ mg_{cat}⁻¹. In this integrated system, NH₃ generation, electrical energy output, and NO gas utilization could be achieved simultaneously. This work provides a new strategy for the design of catalysts for electrocatalytic upgrading of low-concentration NO exhaust gas.

Supporting Information

Supporting Information is available from the Wiley Online Library or from the author.

Acknowledgements

D.W. and G.F. contributed equally to this work. X.W.L. acknowledges the funding support for the Global STEM Professorship from the Innovation, Technology and Industry Bureau ("ITIB") and Education Bureau ("EDB") of Hong Kong.

Conflict of Interest

The authors declare no conflict of interest.

Data Availability Statement

The data that support the findings of this study are available from the corresponding author upon reasonable request.

Keywords

Cu–Co dual-site, electrocatalysis, low-concentration NO, nanobox, NH₃ synthesis

Received: March 6, 2025
Revised: May 9, 2025
Published online:

- [1] P. Ghosh, T. H. Warren, *Nat. Chem.* **2024**, *16*, 1382.
- [2] Y. Tian, J.-C. Gong, C.-Y. Liu, J. Zhang, P.-F. Li, G.-P. Yang, *Environ. Sci. Technol.* **2024**, *58*, 21662.
- [3] X. Liu, S. Li, Z. Ren, H. Cao, Q. Yang, Z. Luo, L. He, J. Zhao, Q. Wang, G. Li, X. Liu, L. Chen, H. Li, D. Zhang, *Environ. Sci. Technol.* **2024**, *58*, 17797.
- [4] W. Qu, X. Liu, J. Chen, Y. Dong, X. Tang, Y. Chen, *Nat. Commun.* **2020**, *11*, 1532.
- [5] J.-J. Chen, S.-D. Wang, Z.-Y. Li, X.-N. Li, S.-G. He, *J. Am. Chem. Soc.* **2023**, *145*, 18658.
- [6] Y. Chen, X. Liu, P. Wang, M. Mansoor, J. Zhang, D. Peng, L. Han, D. Zhang, *JACS Au* **2024**, *4*, 2767.
- [7] X. Tan, P. García-Aznar, G. Sastre, S. B. Hong, *J. Am. Chem. Soc.* **2024**, *146*, 6352.
- [8] B. Wu, L. Huang, L. Yan, H. Gang, Y. Cao, D. Wei, H. Wang, Z. Guo, W. Zhang, *Nano Lett.* **2023**, *23*, 7120.
- [9] S. J. Qian, H. Cao, Y. G. Wang, J. Li, *J. Am. Chem. Soc.* **2024**, *146*, 12530.
- [10] D. Wang, N. He, L. Xiao, F. Dong, W. Chen, Y. Zhou, C. Chen, S. Wang, *Angew. Chem., Int. Ed.* **2021**, *60*, 24605.
- [11] D. Wang, C. Chen, S. Wang, *Sci. China Chem.* **2022**, *66*, 1052.
- [12] S. Zhao, J. Liu, Z. Zhang, C. Zhu, G. Shi, J. Wu, C. Yang, Q. Wang, M. Chang, K. Liu, S. Li, L. Zhang, *Chem* **2023**, *9*, 3555.
- [13] J. Xian, S. Li, H. Su, P. Liao, S. Wang, Y. Zhang, W. Yang, J. Yang, Y. Sun, Y. Jia, Q. Liu, Q. Liu, G. Li, *Angew. Chem., Int. Ed.* **2023**, *62*, 202304007.
- [14] J. Shao, H. Jing, P. Wei, X. Fu, L. Pang, Y. Song, K. Ye, M. Li, L. Jiang, J. Ma, R. Li, R. Si, Z. Peng, G. Wang, J. Xiao, *Nat. Energy* **2023**, *8*, 1273.
- [15] X. Guo, T. Wu, H. Li, L. Chai, M. Liu, *Angew. Chem., Int. Ed.* **2024**, *64*, 202420346.
- [16] S. Li, X. Fu, J. K. Nørskov, I. Chorkendorff, *Nat. Energy* **2024**, *9*, 1344.
- [17] Y. Ren, C. Yu, X. Tan, H. Huang, Q. Wei, J. Qiu, *Energy Environ. Sci.* **2021**, *14*, 1176.
- [18] D. Wang, X. Zhu, X. Tu, X. Zhang, C. Chen, X. Wei, Y. Li, S. Wang, *Adv. Mater.* **2023**, *35*, 2304646.
- [19] W.-Q. Li, M. Xu, J.-S. Chen, T.-N. Ye, *Adv. Mater.* **2024**, *36*, 2408434.
- [20] G. Weng, S. Lei, R. Wang, K. Ouyang, J. Dong, X. Lin, J. Xue, L.-X. Ding, H. Wang, *Joule* **2023**, *7*, 1333.
- [21] X. Zhang, X. Zhu, S. Bo, C. Chen, Q. Zhai, S. Li, X. Tu, J. Zheng, D. Wang, X. Wei, W. Chen, T. Wang, Y. Li, Q. Liu, S. P. Jiang, L. Dai, S. Wang, *Chem* **2024**, *10*, 1516.
- [22] C. Sellers, T. P. Senftle, *Nat. Energy* **2023**, *8*, 1184.
- [23] J. Long, S. Chen, Y. Zhang, C. Guo, X. Fu, D. Deng, J. Xiao, *Angew. Chem., Int. Ed.* **2020**, *59*, 9711.
- [24] D. Wang, X. F. Lu, D. Luan, X. W. Lou, *Adv. Mater.* **2024**, *36*, 2312645.
- [25] C. Li, Y. Wang, X. Wang, T. Azam, Z.-S. Wu, *Chem* **2024**, *10*, 2666.
- [26] J. Zhou, S. Han, R. Yang, T. Li, W. Li, Y. Wang, Y. Yu, B. Zhang, *Angew. Chem., Int. Ed.* **2023**, *62*, 202305184.
- [27] R. Hao, L. Tian, C. Wang, L. Wang, Y. Liu, G. Wang, W. Li, G. A. Ozin, *Chem. Catal.* **2022**, *2*, 622.
- [28] D. Kim, D. Shin, J. Heo, H. Lim, J.-A. Lim, H. M. Jeong, B.-S. Kim, I. Heo, I. Oh, B. Lee, M. Sharma, H. Lim, H. Kim, Y. Kwon, *ACS Energy Lett.* **2020**, *5*, 3647.
- [29] H. Zhang, Y. Li, C. Cheng, J. Zhou, P. Yin, H. Wu, Z. Liang, J. Zhang, Q. Yun, A.-L. Wang, L. Zhu, B. Zhang, W. Cao, X. Meng, J. Xia, Y. Yu, Q. Lu, *Angew. Chem., Int. Ed.* **2023**, *62*, 202213351.
- [30] J. Shi, C. Wang, R. Yang, F. Chen, N. Meng, Y. Yu, B. Zhang, *Sci. China Chem.* **2021**, *64*, 1493.
- [31] B. S. Patil, F. J. J. Peeters, G. J. van Rooij, J. A. Medrano, F. Gallucci, J. Lang, Q. Wang, V. Hessel, *AIChE J.* **2018**, *64*, 526.
- [32] Y. Li, C. Cheng, S. Han, Y. Huang, X. Du, B. Zhang, Y. Yu, *ACS Energy Lett.* **2022**, *7*, 1187.
- [33] X. Guo, P. Wang, T. Wu, Z. Wang, J. Li, K. Liu, J. Fu, M. Liu, J. Wu, Z. Lin, L. Chai, Z. Bian, H. Li, M. Liu, *Angew. Chem., Int. Ed.* **2024**, *63*, 202318792.
- [34] Z. Wu, Y. Liu, D. Wang, Y. Zhang, K. Gu, Z. He, L. Liu, H. Liu, J. Fan, C. Chen, S. Wang, *Adv. Mater.* **2024**, *36*, 2309470.
- [35] J. Meng, C. Cheng, Y. Wang, Y. Yu, B. Zhang, *J. Am. Chem. Soc.* **2024**, *146*, 10044.
- [36] D. Wang, G. Fan, D. Luan, Y. Guo, X. Gu, X. W. Lou, *Adv. Mater.* **2024**, *36*, 2408580.
- [37] D. Wang, Z.-W. Chen, K. Gu, C. Chen, Y. Liu, X. Wei, C. V. Singh, S. Wang, *J. Am. Chem. Soc.* **2023**, *145*, 6899.
- [38] Y. Fang, D. Luan, S. Gao, X. W. Lou, *Angew. Chem., Int. Ed.* **2021**, *60*, 20102.
- [39] X. Wang, Y. Chen, Y. Fang, J. Zhang, S. Gao, X. W. Lou, *Angew. Chem., Int. Ed.* **2019**, *58*, 2675.
- [40] D. Wang, Z. Liu, S. Du, Y. Zhang, H. Li, Z. Xiao, W. Chen, R. Chen, Y. Wang, Y. Zou, S. Wang, *J. Mater. Chem. A* **2019**, *7*, 24211.
- [41] Y. Zhai, C. Jin, Q. Xia, W. Han, J. Wu, X. Zhao, X. Zhang, *Adv. Funct. Mater.* **2024**, *34*, 2311063.
- [42] T. Zhang, B. Yuan, W. Wang, J. He, X. Xiang, *Angew. Chem., Int. Ed.* **2023**, *62*, 202302096.
- [43] Z. Wang, J. Huang, L. Wang, Y. Liu, W. Liu, S. Zhao, Z.-Q. Liu, *Angew. Chem., Int. Ed.* **2022**, *61*, 202114696.
- [44] Y. Zhu, J. Wang, T. Koketsu, M. Kroschel, J.-M. Chen, S.-Y. Hsu, G. Henkelman, Z. Hu, P. Strasser, J. Ma, *Nat. Commun.* **2022**, *13*, 7754.
- [45] B. Kang, B. Xu, Z. Chen, F. Li, Y. Wang, *Appl. Catal. B* **2025**, *360*, 124528.
- [46] P. Guo, D. Luan, H. Li, L. Li, S. Yang, J. Xiao, *J. Am. Chem. Soc.* **2024**, *146*, 13974.
- [47] P. Zhang, K. Chen, J. Li, M. Wang, M. Li, Y. Liu, Y. Pan, *Adv. Mater.* **2023**, *35*, 2303243.
- [48] W. Yu, Y. Wang, H. Tan, M. Huang, J. Yu, L. Chen, J. Wang, H. Liu, W. Zhou, *Adv. Energy Mater.* **2024**, *14*, 2402970.